Motion and Evolution of Oceanic Rings in a Numerical Model and in Observations

ERIC P. CHASSIGNET [1]

National Center for Atmospheric Research, Boulder, Colorado

DONALD B. OLSON AND DOUGLAS B. BOUDRA [2]

Rosenstiel School of Marine and Atmospheric Science, Miami, Florida

Observed properties of oceanic rings are compared to rings produced in a two-gyre wind-driven numerical ocean model and in a model of the South Atlantic/Indian Ocean. Their temporal evolution is discussed in terms of structure and translation rate. They exhibit substantial similarity in terms of thermocline depth, ring size, swirl velocities, and translations speeds. In both observations and numerical model results, the propagation speeds are 2 to 5 times faster than that of an equivalent isolated eddy (which is of the order of the long Rossby wave speed). This is attributed to advection by the mean flows. Furthermore, it is observed that the model rings have a coherent structure all the way to the bottom. There is strong evidence that this is also the case in real oceanic rings. One major difference between observed and modeled rings is in their decay rate. The temporal decay of the rings in the models and observations is therefore discussed in relation to the decay mechanisms at work and the frictional parameterization of the model.

1. INTRODUCTION

The temporal evolution of rings has been described in models where isolated vortices are placed on a β plane [*McWilliams and Flierl*, 1979; *Meid and Lindemann*, 1979] and in several long term field observations [*Cheney and Richardson*, 1976; *Vastano et al.*, 1980; *Joyce et al.*, 1984; *Olson et al.*, 1985]. There have not been any detailed intercomparisons, however, between these observed rings and the model results, nor have rings produced by gyre scale simulations of the ocean been examined in relation to isolated model rings or observations. The early models used amplitudes of ring layer depth and velocities characteristic of very weak observed rings. Recent primitive equation model experiments have included more realistic ring simulations and thus prompted the comparison made here.

Oceanic rings have been extensively surveyed in the past 20 years, mostly for short periods because of the extensive amount of ship time required for long-term observations. Thus the comparison first considers 34 ring surveys from various western boundary currents and several representative model rings. Then, the long time evolution of the model rings is discussed in relation to the few long time series of observed rings that we have at our disposition. *Cheney and Richardson* [1976] tracked a cyclonic Gulf Stream ring in the Sargasso sea in five cruises from March 1971 to April 1972. The ring was observed to move 700 km southwest at about $2\,\mathrm{km\,day^{-1}}$ before coalescing with the Gulf Stream off Cape Canaveral.

The temporal evolution of another cyclone (ring BOB) was described by *Vastano et al.* [1980] and *Olson* [1980], but for only a few months. The longest description of an anticyclonic ring is the survey of Ring 82B described in detail by *Joyce et al.* [1984] and *Olson et al.* [1985] which covers a period of 6 months from March to August of 1982, with six full coverages of the ring. Discussion of the time evolution of a Gulf of Mexico Loop Current ring and of a cyclonic ring in the Antarctic Circumpolar Current can be found in the papers by *Elliot* [1982] and *Joyce et al.* [1981]. Finding an agreeable amount of similarity between observed and modeled rings then provides the opportunity and justification to isolate in the numerical model the possible factors influencing the observed ring motion and evolution, which is not possible with observations alone.

The observations use a diagnostic two-layer model fully described by *Olson et al.* [1985] and *Olson and Evans* [1986]. The diagnostic model, which makes use of observed thermocline depths, is compared to the multilayer quasi-isopycnic coordinate numerical model developed by *Bleck and Boudra* [1981], which is used in the simulations. The model is configured in a square basin and in an idealized South Atlantic/Indian Ocean basin, and characteristic rings are selected from each configuration.

The layout of the paper is as follows. In section 2, the model characteristics are reviewed and the primary numerical experiments are briefly described. Section 3 compares modeled and observed rings in terms of ring structure, ring translation, ring parameters (Rossby number, Burger number, etc.) and ring energetics. In section 4, special attention is given to the ring motion and evolution and a number of subsidiary experiments help to identify and to quantify the primary factors influencing them. The final discussion in section 5 considers both (1) the general similarity of the observed and model rings and (2) the temporal decay in the models and observations in relation to the decay mechanisms at work and the frictional parameterization in the model.

[1] Now at Rosenstiel School of Marine and Atmospheric Sciences, Miami, Florida.
[2] Deceased.

2. DESCRIPTION OF THE MODEL AND EXPERIMENTS

2.1. The Model

The numerical model used in this paper is the *Bleck and Boudra* [1981] quasi-isopycnic coordinate, primitive equation model. This model incorporates the rigid lid approximation and employs an Arakawa C-grid configuration. Vorticity and horizontal velocities are defined as mean layer properties. Pressure and geopotential are defined at the interfaces. The advantages of the coordinate system of the model are (1) that vertical resolution is concentrated in regions of strong horizontal density gradients and (2) that lateral diffusion is along isopycnal surfaces, where mixing of material properties by eddies in the stably stratified parts of the oceans mostly occurs [*Iselin*, 1939; *Montgomery*, 1940; *Gent and McWilliams*, 1990]. The model is therefore free of any artificial deterioration of stratification or baroclinicity due to cross-isopycnal numerical diffusion.

The equations for the model are

Momentum equation

$$\left(\frac{\partial \mathbf{V}}{\partial t}\right)_s = -\frac{\nabla_s \mathbf{V}^2}{2} - (\zeta_s + f)\mathbf{k} \times \mathbf{V} -$$

$$\left(\dot{s}\frac{\partial p}{\partial s}\right)\frac{\partial \mathbf{V}}{\partial s} - \alpha\nabla_s p - \nabla_s\phi +$$

$$\alpha\frac{\partial \vec{\tau}}{\partial z} + A_M\left(\frac{\partial p}{\partial s}\right)^{-1}\nabla_s\cdot\left(\frac{\partial p}{\partial s}\nabla_s\mathbf{V}\right) \quad (1)$$

where s is the generalized vertical coordinate, $\dot{s} = ds/dt$, α is the specific volume (ρ^{-1}), ϕ is the geopotential, A_M is the lateral eddy viscosity, and the other symbols are conventional. The subscript s indicates derivatives on surfaces of constant s.

Continuity equation

$$\frac{\partial}{\partial t}\left(\frac{\partial p}{\partial s}\right) + \nabla_s\cdot\left(\mathbf{V}\frac{\partial p}{\partial s}\right) + \frac{\partial}{\partial s}\left(\dot{s}\frac{\partial p}{\partial s}\right) = 0 \quad (2)$$

Hydrostatic equation

$$\frac{\partial \phi}{\partial s} = -\alpha\left(\frac{\partial p}{\partial s}\right) \quad (3)$$

The differential form of the primitive equations in the absence of forcing and dissipation conserves potential enstrophy and potential vorticity. In this model, the finite difference formulation of the nonlinear terms is such that those properties are rigorously conserved (see *Bleck* [1979] for more detail). The conversion to finite difference formulation as well as the testing of the model are described in detail by *Bleck and Boudra* [1981].

The model is configured in a three-layer formulation in a square flat-bottom basin experiment (referred to as 2G) similar to that of *Holland* [1978] and in an idealized South Atlantic-Indian Ocean flat-bottom basin experiment (referred to as E11). Both model configurations are driven by a steady zonal wind stress, which has a sinusoidal meridional variation. The parameters for the experiments are given in Table 1.

For the double-gyre experiment (2G), the applied wind stress is $\tau_x = -\tau_m \cos(2\pi y/L)$ where $\tau_m = 1 \times 10^{-4}\text{m}^2\text{s}^{-2}$ and $L = 2000$ km. The resulting circulation pattern is nearly anti-symmetric about mid-latitude, with a counterclockwise gyre north of the wind stress curl zero and clockwise south. The upper layer mean mass transport stream function is presented in Figure 1a. The boundary conditions are free-slip everywhere. Meanders develop within the free jet and grow in time, resulting eventually in eddy detachment. For more detail, the reader is referred to *Holland* [1978].

In the South Atlantic/Indian Ocean experiment (E11), the applied wind stress is $\tau_x = \tau_m \cos(\pi(y - a)/L)$ where $\tau_m = 2 \times 10^{-4}\text{m}^2\text{s}^{-2}$, $L = 1000$ km and $a = 280$ km. The resulting circulation pattern includes anticyclonic subtropical gyres in the Atlantic and Indian sectors, respectively, and an elongated cyclonic subpolar gyre south of the wind curl zero. Africa is represented by a triangular shape, approximating that of the Agulhas Bank shelf break. The upper layer mean mass transport stream function is shown in Figure 1b. The boundary conditions are no-slip on meridional boundaries, including all of Africa, and free-slip on zonal boundaries. The intense boundary current along the eastern coast of Africa constitutes the Agulhas Current and the major part of it retroflects south of the tip of Africa, returning eastward toward the Indian Ocean. In turning back, several times a year the Agulhas intercepts itself and forms a ring which translates into the

TABLE 1. Parameters of Experiments 2G and E11

Experiment	Number of Layers	Thickness of Layers, m	g', m s^{-2}	Bottom drag, s^{-1}	Basin size, km × km
2G	3	400	0.018	10^{-7}	2000 × 2000
		1600	0.003		
		3000			
E11	3	300	0.02		2520 × 1280
		900	0.005		
		3800			

For both experiments, $\Delta x = 20$ km and $A_M = 330$ m^2 s^{-1}. Blanks indicate no change from the previous experiment.
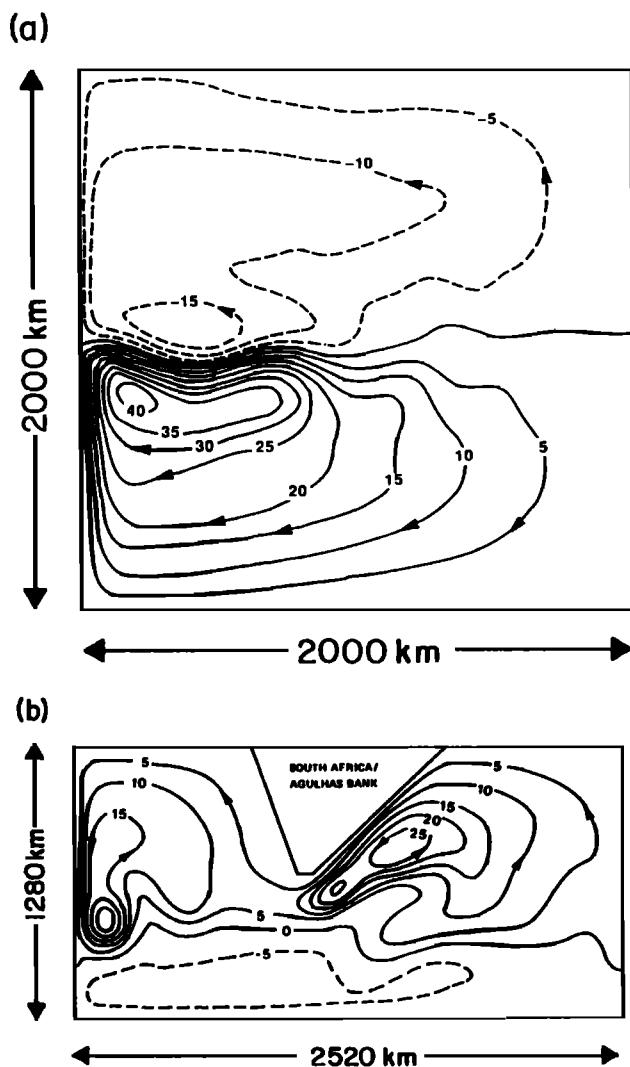
(a)

◀——— 2000 km ———▶

(b)

◀——————— 2520 km ———————▶

Fig. 1. Upper layer mean mass transport stream function of (a) 2G and (b) E11. The contour interval is 5 Sv (1 Sv = $10^6 m^3 s^{-1}$).

Fig. 2. Ring trajectories in experiment 2G for a 10-year period.

Atlantic. For more details on this experiment, see *Boudra and Chassignet* [1988] and *Chassignet and Boudra* [1988].

2.2. Description of Double-Gyre Model Rings 2G1, 2G2, and 2G3

In this double-gyre experiment, most cyclones (cold-core rings or CCRs) have the tendency to form at the middle of the jet extension while anticyclones (warm-core rings or WCRs) form either at the same position as the CCRs or at the jet's end. Once formed, the ring propagation is almost westward along the mean position of the mid-latitude jet (Figure 2). The number of rings found in the model is low when compared to the observations of *Brown et al.* [1986] based on a time series of satellite infrared determinations of Gulf Stream rings. Over the 10-year period, 1.4 WCRs and CCRs per year were observed to form in the model versus eight WCRs reported by *Brown et al.* [1986].

Three rings were selected for the comparison as representative of the above statistical study. Two warm-core rings are chosen from near the end of the 7200 day simulation.
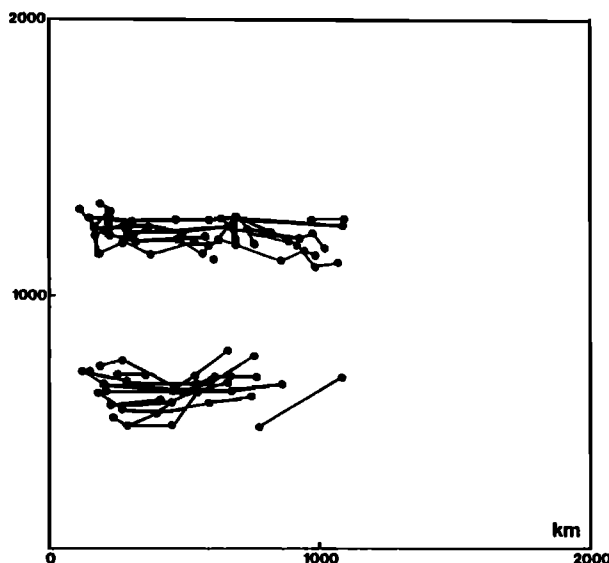
At day 6160 (Figure 3a), the first ring, which we call 2G1, has just separated from the free jet and the second (2G2) is forming. The time evolution for the two rings is illustrated in Figure 3 for a period of 80 days. At day 6160, the shape of 2G1 is quite elongated and it is only at day 6180 (Figure 3b) that the ring becomes more symmetric. Ring 2G1 keeps this quasi-circular shape until day 6210 (Figure 3c) when the ring starts to interact with the western boundary of the basin. The propagation speed of 2G1 until day 6210 is approximately $9 \, cm \, s^{-1}$ in the westward direction with a very small northward propagation. Ring 2G2 (Figure 3d) separates around day 6180 with a fairly circular shape and interacts with the free jet until day 6210. Ring 2G2 moves westward at approximately the same speed as 2G1 until day 6240 (Figure 3d) where it encounters the now-weakened 2G1.

The diameters of the rings 2G1 and 2G2 just after formation are approximately the same (between 250 and 300 km), their maximum velocities of the order of 60 and $80 \, cm \, s^{-1}$ (2G2 and 2G1, respectively) at a radius of about 70 km and a maximum interface displacement at the center between 250 and 300 m. In 50 days the diameters and interface displacements at the center remain almost unchanged. There is first an increase in the maximum velocities to $100 - 120 \, cm \, s^{-1}$ (2G2 and 2G1, respectively), followed by a decrease to $60 - 80 \, cm \, s^{-1}$. Rapid decay ensues when the rings reach the western boundary.

The third ring is a cold-core ring (2G3), which forms around day 5760, and its time evolution is presented in Figure 4 for a period of 80 days. After its formation, 2G3 moves slowly westward and interacts with the mid-latitude jet until day 5810 where it becomes isolated. Its shape then becomes circular (Figure 4c). Its westward propagation speed until day 5810 is approximately $6 \, cm \, s^{-1}$ which increases to $11 \, cm \, s^{-1}$ when away from the stream. The diameter of 2G3 remains almost unchanged (250 km) until it reaches the western boundary. The maximum velocity on the contrary varies from 80 to $60 \, cm \, s^{-1}$ at a radius of about 70 km while the maximum interface displacement at the center varies from 330 to 260 m.

DAY 6160 **(a)**   **DAY 6180** **(b)**
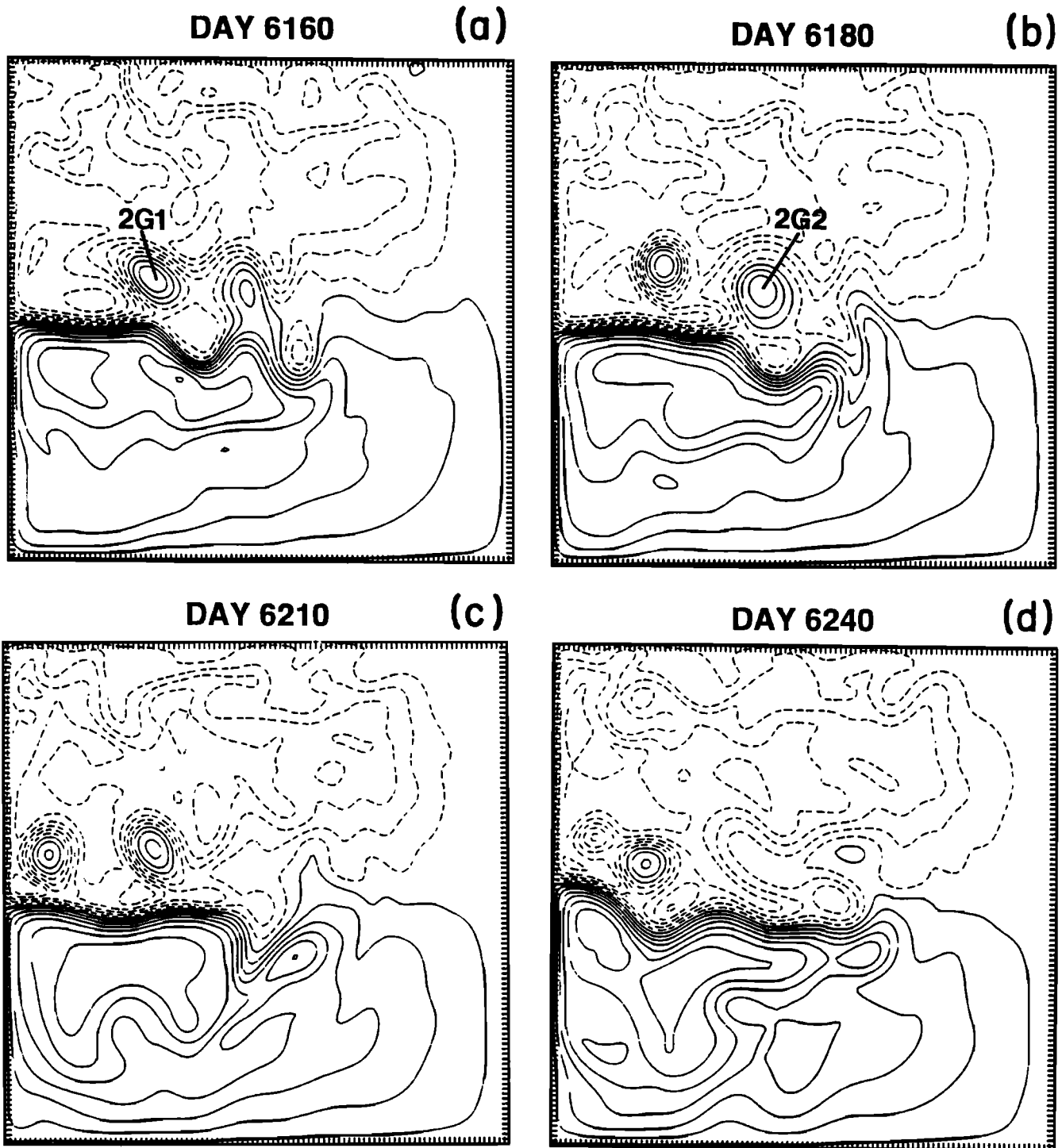
DAY 6210 **(c)**   **DAY 6240** **(d)**

Fig. 3. Time evolution of the upper depth interface anomaly field of 2G for 2G1 and 2G2 from day 6160 to day 6240. The contour interval is 20 m and the contour values straddle zero symmetrically. The distance between each tick mark is 20 km.

2.3. Description of Simulated Agulhas Ring RE11

There are a number of situations in the ocean where rings are formed by intrusion process, such as, for example, the Gulf of Mexico Loop Current [Elliot, 1982], the East Australian current [Nilsson and Cresswell, 1980] and the case simulated here, the Agulhas current [Olson and Evans, 1986]. A frequency of three to five rings per year was observed in a dataset of 4 years of infrared measurements of the sea surface temperature processed by the Remote Sensing Group of the University of Miami. This is less than the estimate of Lutjeharms and van Ballegooyen [1988] (six to eight rings per year), but is in accordance with a study of altimeter data from Gordon and Haxby [1990] which suggests a production rate of about five rings per

DAY 5770   (a)

DAY 5790   (b)

DAY 5810   (c)

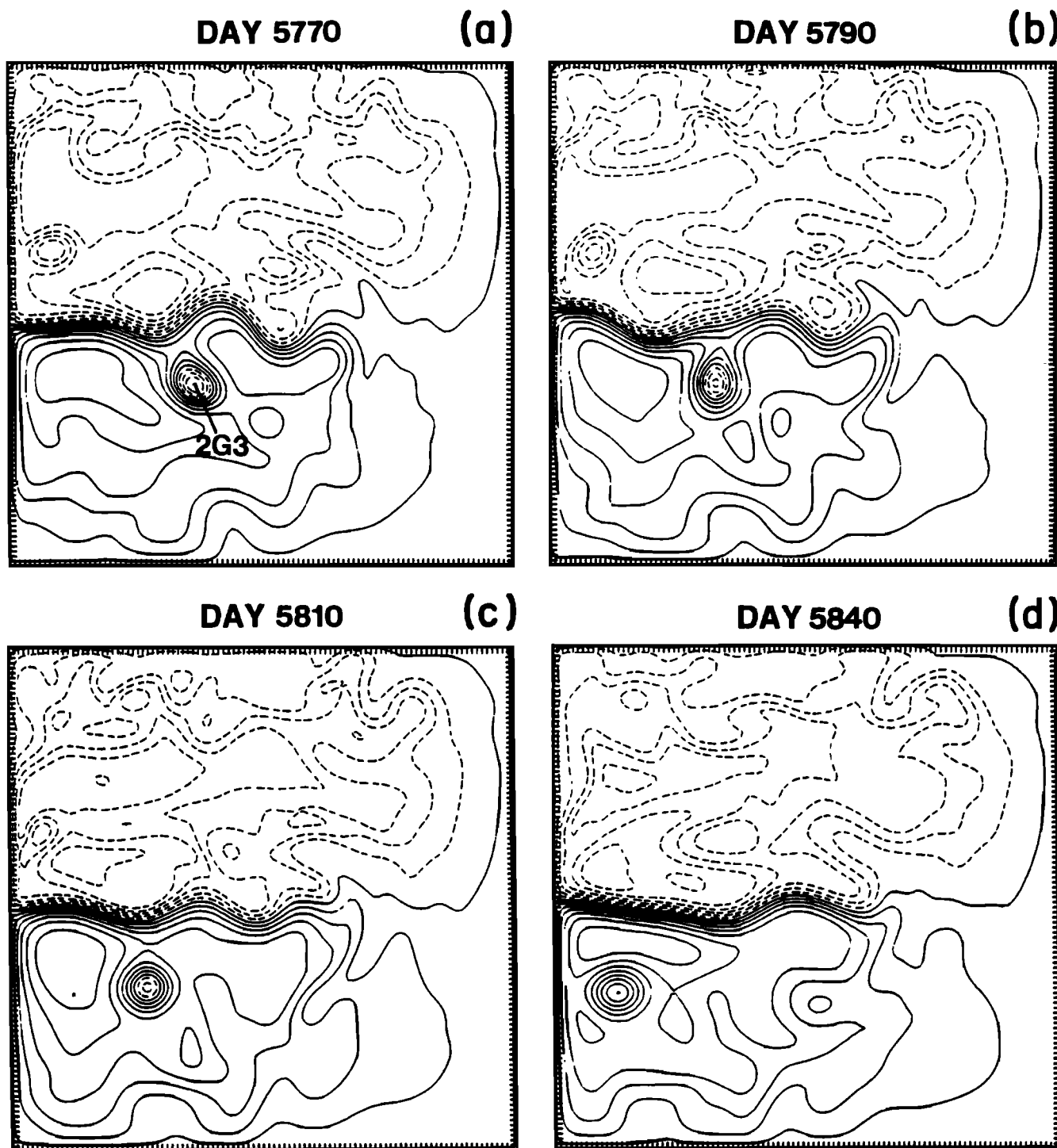## DAY 5840   (d)

Fig. 4. Same as in Figure 3 for 2G3 from day 5770 to day 5840.

year. The numerical model produced an average of three rings per year.

In experiment E11, ring RE11 forms around day 2950 (beginning of year 9 from a 10-year simulation), and the time evolution of its upper interface depth anomaly field is illustrated in Figure 5, for a period of 90 days. Rings in E11 form along the coast of Africa at a rate of two to three per year. The formation process for this ring is

described in detail by *Chassignet and Boudra* [1988]. At day 2955 (Figure 5a), the ring has just separated from the Agulhas proper and moves in a southwestward direction. The shape is quite symmetric, but on its northern side some deformation occurs because of the presence of the African continent. As the ring rounds the tip of Africa, it is compressed between the continent and the return flow from the Atlantic basin. The ring's shape becomes

DAY 2955   (a)

DAY 2975   (b)

DAY 2995   (c)

DAY 3015   (d)
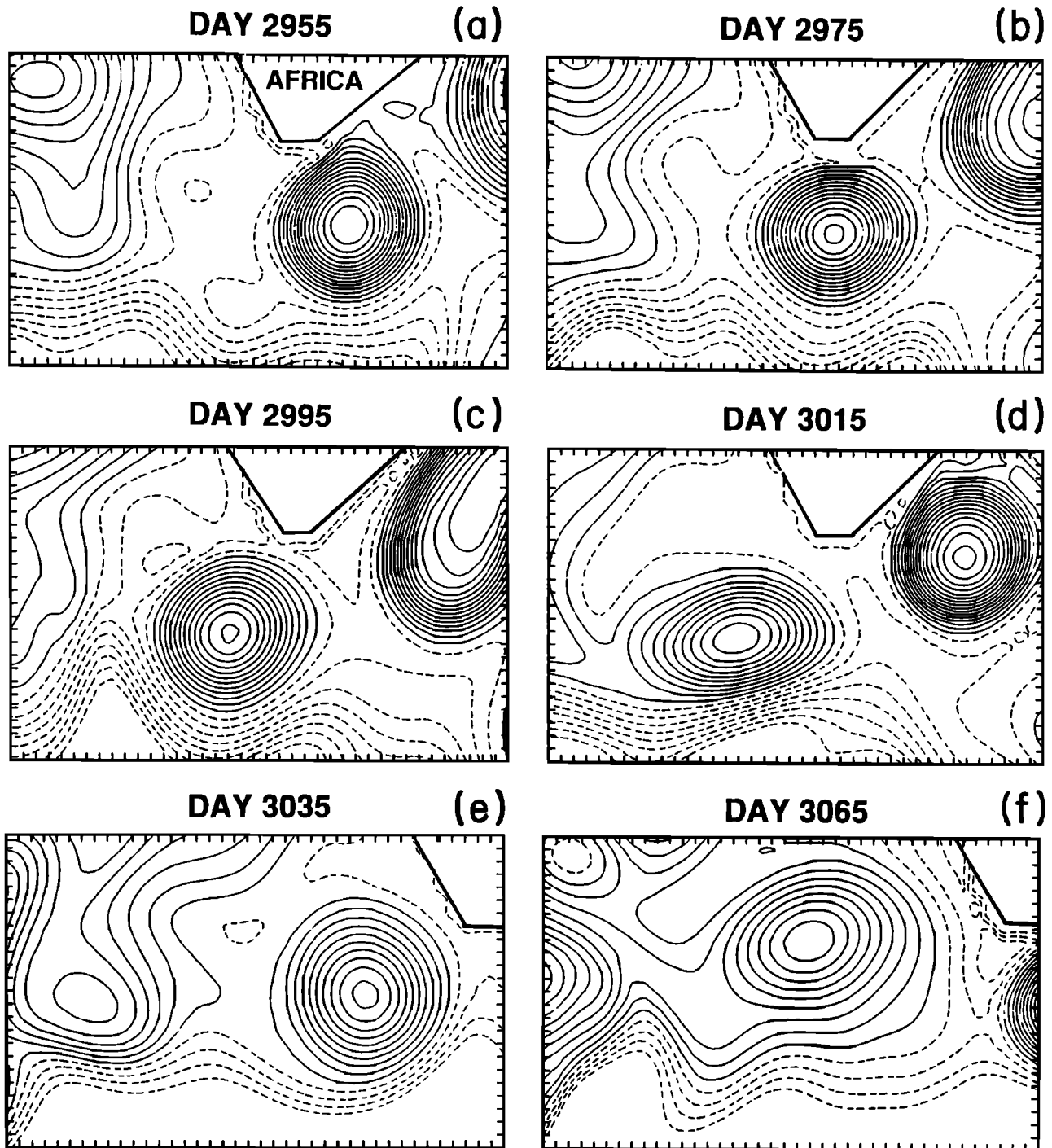
DAY 3035   (e)

DAY 3065   (f)

Fig. 5. Same as in Figure 3 for RE11 from day 2955 to day 3065. The two last frames are shifted westward.

elliptic and undergoes strong deformation as it propagates westward (Figures 5b-5d). At day 3035 (Figure 5e), once the ring has escaped from the influence of Africa, it regains a more circular shape and starts to move toward the west-northwest. It then gets slowly absorbed by the South Atlantic subtropical gyre (Figure 5f). The propagation speed of the ring until day 3025 (when moving westward) is approximately $4.3 \, \text{cm} \, \text{s}^{-1}$. The speed then increases to $6.2 \, \text{cm} \, \text{s}^{-1}$ in the northwestward direction ($5.5 \, \text{cm} \, \text{s}^{-1}$ toward the west and $2.8 \, \text{cm} \, \text{s}^{-1}$ toward the north).

At day 2955 the ring diameter is of the order of 300 km, the maximum velocities of $120 \, \text{cm} \, \text{s}^{-1}$ at a radius of about 80 km and the interface displacement at center of 300 m. In 50 days, the diameter remains approximately unchanged, but the magnitude of the velocities has dropped by about 45% to $75 \, \text{cm} \, \text{s}^{-1}$ and the interface displacement at the center to 260 m. The greatest loss in amplitude seems to occur between day 2995 and 3035, when the ring undergoes strong deformation from a circular shape to elliptic and then back to circular.

3. COMPARISONS WITH OBSERVATIONS

3.1. Ring Structures

The physical structure of rings from various boundary currents around the world can be compared in a uniform manner through the use of a simple two-layer approximation of their first baroclinic structure. This approach is fully described by *Olson et al.* [1985], whose chosen interface corresponds to the best fit to the main thermocline of the ring. The model stratifications in the present study (Table 1) are chosen such that the first interface lies, in general, in the upper portion of the main thermocline, allowing a realistic level of nonlinearity and baroclinicity in the upper part of the model ocean circulation. A quantitative comparison is obtained when properly scaled parameters are used.

Once formed, an oceanic ring should evolve in time and reach an approximate gradient balance state

$$\frac{v^2}{r} + fv = g'\frac{\partial h}{\partial r} \qquad (4)$$

where v is the azimuthal velocity and $\partial h/\partial r$ the radial derivative of the interface depth h. Equation (4) is derived for a symmetric ring from the equations of motion for an inviscid fluid in a cylindrical coordinate system associated with the ring:

$$\frac{\partial u}{\partial t} + u\frac{\partial u}{\partial r} - \frac{v^2}{r} + \frac{v}{r}\frac{\partial u}{\partial \theta} + w\frac{\partial u}{\partial z} - fv = -\frac{1}{\rho}\frac{\partial p}{\partial r} \qquad (5)$$

$$\frac{\partial v}{\partial t} + \frac{vu}{r} + u\frac{\partial v}{\partial r} + \frac{v}{r}\frac{\partial v}{\partial \theta} + w\frac{\partial v}{\partial z} + fu = -\frac{1}{\rho r}\frac{\partial p}{\partial \theta} \qquad (6)$$

$$\frac{\partial w}{\partial t} + u\frac{\partial w}{\partial r} + \frac{v}{r}\frac{\partial w}{\partial \theta} + w\frac{\partial w}{\partial z} = -\frac{1}{\rho}\frac{\partial p}{\partial z} - g \qquad (7)$$

where u, v, and w are the radial (r), azimuthal (θ), and vertical (z) velocities, respectively, p is the pressure, and ρ is the density. If the ring is perfectly symmetric, $u = 0$ and then (4) is satisfied. If the ring is strongly out of balance, then the other terms in (5) and (6) might start to play a significant role. An analysis of the magnitude of this effect on an elliptical ring with mean and fluctuating velocities representative of the rings studied suggested that the error induced is only of the order of 1%.

Common practice for the scaling of rings is to consider the length scale L as the radius of maximum swirl velocity and the velocity scale V as the maximum velocity V_{max} [*Olson*, 1980]. If the ring is considered as consisting of two fluid layers with different densities [*Olson et al.*, 1985], we can define a Burger number $B' = g'\Delta h/f^2 L^2$ for the change in interface height across the ring and the scaling of (4) leads to

$$R_o^2 + R_o = B' \qquad (8)$$

where $R_o = V/fL$ is the Rossby number for the gradient flow. This scaling allows intercomparisons between different rings.

The above numbers were computed for a set of 34 observed rings from the world ocean and their characteristics are compiled in Table 2. Equation (8) (R_o versus B') is represented in Figure 6 and each dot corresponds to one

TABLE 2. Scaled Parameters of 34 Observed Rings From the World Ocean.

Ring		V_{max}, cm s^{-1}	L, km	B'	B	R_o
		Gulf Stream				
1	WCR81D 9/81	-2.00	83	-0.06	0.08	-0.16
2	WCR81D 9/81	-1.50	55	-0.08	0.13	-0.29
3	WCR82B 3/82	-0.41	55	-0.14	0.15	-0.08
4	WCR82B 4/82	-0.55	55	-0.14	0.16	-0.11
5	WCR82B 6/82	-0.55	55	-0.15	0.16	-0.12
6	WCR82B 7/82	-0.51	35	-0.25	0.38	-0.19
7	WCR82B 8/82	-0.43	45	-0.13	0.23	-0.11
8	WCR82B 8/82	-0.22	35	-0.11	0.31	-0.07
9	CCR AT35 67	1.25	45	0.37	0.47	0.32
10	CCR AT38 67	1.00	45	0.45	0.43	0.26
11	CCR 71294	1.63	50	0.48	0.44	0.43
12	CCR 71312	0.87	80	0.13	0.18	0.13
13	CCR 72306	1.04	40	0.48	0.81	0.34
14	CCR 75119	0.74	60	0.26	0.33	0.15
15	CCR 75157	1.37	50	0.47	0.42	0.32
16	CCR 75152	0.51	30	0.46	1.74	0.25
17	CCR 75342	1.15	50	0.44	0.39	0.35
18	CCR 76264	0.69	50	0.29	0.53	0.18
19	CCR 77209	0.95	30	1.00	1.55	0.44
20	CCR Bob	1.49	53	0.46	0.33	0.34
21	CCR Al	0.65	70	0.16	0.20	0.11
22	CCR Franklin	1.98	60	0.35	0.29	0.42
23	CCR Emmerson	0.77	40	0.53	0.65	0.23
		Kuroshio				
24	CCR Cheney	0.80	60	0.26	0.25	0.19
25	WCR 7/71	-0.62	75	-0.11	0.14	-0.09
26	WCR 8/72	-1.21	105	-0.10	0.07	-0.13
		East Australia				
27	WCR 9/74	-0.96	75	-0.06	0.07	-0.15
28	WCR 12/76	-1.00	95	-0.09	0.09	-0.12
		Brazil/Malvinas				
29	CCR 10/84	0.53	135	0.04	0.04	0.04
30	WCR 10/84 1	-0.36	55	-0.09	0.14	-0.06
31	WCR 10/84 2	-0.77	65	-0.09	0.07	-0.11
		Agulhas				
32	WCR 11/83 1	-0.60	115	-0.08	0.12	-0.04
33	WCR 11/83 2	-0.90	130	-0.06	0.07	-0.07
		Gulf of Mexico				
34	1967	-0.88	149	-0.05	0.06	-0.10

ring of Table 2. Anticyclones are required from (8) to have a Burger number greater than -0.25, and all the observed anticyclones satisfy this criterion (Figure 6). Moreover, most of them are located close to the gradient balance curve. The cyclones do not have such a requirement and the scatter along the curve is bigger.

In order to place the model rings in Figure 6, one has to know how the depth of the first interface of the model rings compares to available observations. In order to address this question, the radial distribution of the depth of the first
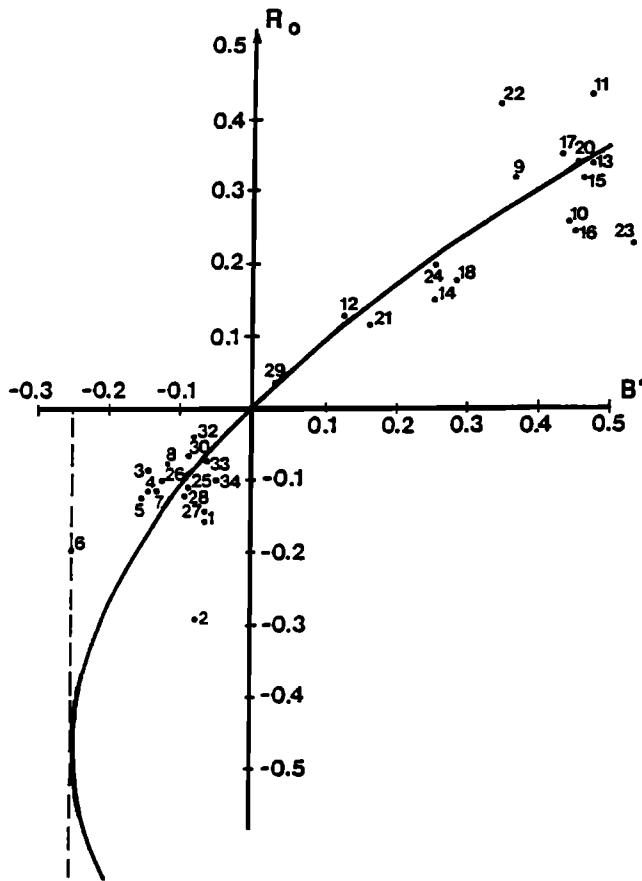
Fig. 6. Representation of the Rossby number (R_o) for the gradient flow versus the Burger number (B') for the change in interface height across the ring (solid line). Compilation of 34 observed world oceanic rings listed in Table 2.
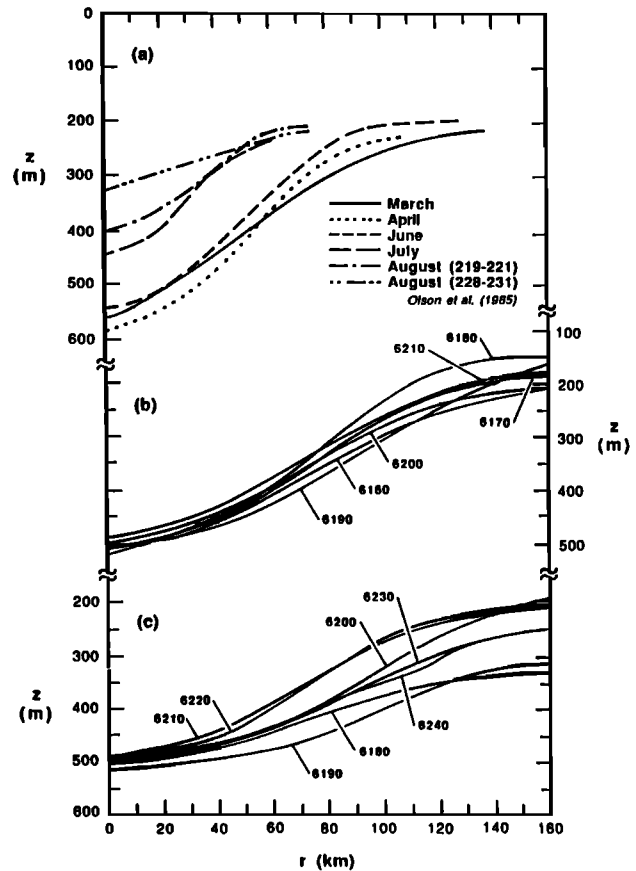
Fig. 7. Radial distributions of the depth (a) of the 10°C isotherm from Gulf Stream warm core ring 82B [from *Olson et al.*, 1985] and of the first interface from (b) 2G1 (day 6160-6210) and (c) 2G2 (day 6180-6240).

interface from the model rings 2G1, 2G2, 2G3, and RE11 and of the main thermocline of Gulf Stream warm-core ring 82B [*Olson et al.*, 1985], cold-core ring CCR76 [*Cheney and Richardson*, 1976] and two Agulhas rings [*Olson and Evans*, 1986] are compared. The chosen isotherm surfaces represents the best fit to the main thermocline of the observed rings studied.

The first three profiles of 82B (March-June 1982) were taken when the ring was not interacting with the Gulf Stream, the last three when the ring was in contact (Figure 7a). In comparison with ring 82B, both 2G1 and 2G2 have a smaller interface displacement at the center (of the order of 50 m), but the major differences appear in ring diameter (~ 160 km for 82B, 200-300 km for 2G1 and 2G2) (Figure 7) and in volume (Table 3). Ring 82B has velocity maxima between 30 and $70 \, \mathrm{cm \, s^{-1}}$ at a radius of about 50 km versus between 60 and $120 \, \mathrm{cm \, s^{-1}}$ at a radius of about 70 km for 2G1 and 2G2. In comparison with CCR76 (not represented), 2G3 has a smaller interface displacement at the center, but as 2G1 and 2G2, the major difference is in ring diameter (~ 110-160 km for CCR76 versus 250 km for 2G3). On the other hand, the maximum velocities are of comparable magnitude.

Differences between RE11 at day 2955 (just after formation when most vigorous) and the observed Agulhas rings (Figure 8) are a smaller interface depth of 100-150

m for the model ring and less volume (Table 3). A choice of a shallower isotherm than $10^\circ C$ or of a thicker upper layer (400 m at rest, as in 2G, instead of 300 m) might provide a better agreement between the model and observations. Both observed rings have velocity maxima between 110 and 130 km from center (80 km for RE11). The newer, southern ring (referred to as the Retroflection eddy in Table 3) is more intense, with maximum velocities of nearly $90 \, \mathrm{cm \, s^{-1}}$ (between 75 and $120 \, \mathrm{cm \, s^{-1}}$ for RE11) as compared to approximately $60 \, \mathrm{cm \, s^{-1}}$ in the northern ring, referred to as the Cape Town eddy [*Olson and Evans*, 1986].

The above intercomparison between simulated and observed rings therefore depends strongly on the variables chosen, such as interface depth, but nevertheless, a general agreement is obtained in terms of structure. When the first interface is considered in the computation of B' for the model rings, 2G1, 2G2, 2G3, and RE11 are observed to be well located among the majority of the world anticyclonic and cyclonic rings in the Rossby-Burger plane. Their time evolutions are represented in Figures 9a and 9b. Rings 2G1 and 2G2 do not show a very organized pattern in their time evolution (Figure 9a), probably because of strong interactions with the nearby jet. It appears to be also the case for 82B and CCR76 (dots 3 to 8 and 11 to 13 in Figure 7, respectively). On the contrary, both 2G3 and

TABLE 3. Available Potential Energy, Kinetic Energy and Volume, When Available, for Various Rings.

Ring	$P \times 10^{15} J$	$K \times 10^{15} J$	Volume $\times 10^{12}$ m³
2G1	12.3	5.9	4.3
2G2	10.0	6.8	6.0
2G3	12.5	7.5	5.3
82B	4.2	1.0	3.9
CCR76	8.0		
RE11	16.0	7.0	8.3
Retroflection eddy	51.4	8.7	19.2
Cape Town eddy	30.5	6.2	15.2

Values for 2G1 are at day 6160, 2G2 at day 6210, 2G3 at day 5770, and RE11 at day 2955. The data for Gulf Stream warm core ring 82B are from *Olson et al.* [1985], from *Cheney and Richardson* [1976] for Gulf Stream cold core ring CCR76, and from *Olson and Evans* [1986] for the two Agulhas rings.
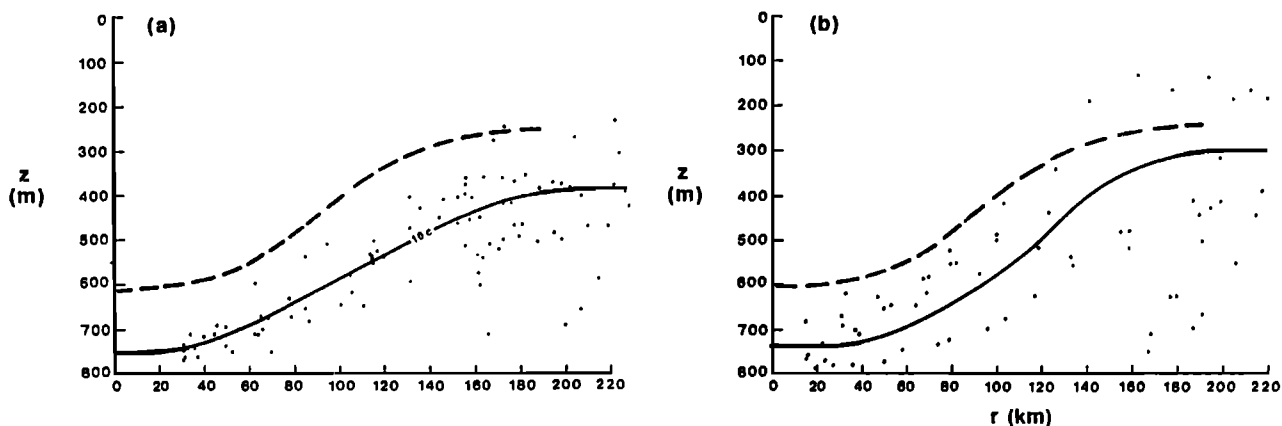

Fig. 8. Radial distribution of the depth of the first interface from RE11 at day 2955 (dashed line) and of the 10°C isotherm (solid line) in (a) the northern and (b) the southern observed Agulhas rings [from *Olson and Evans*, 1986].
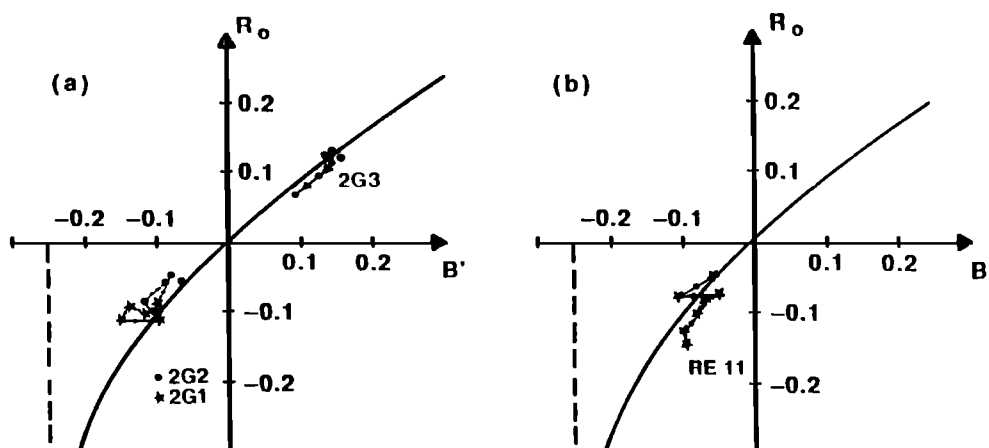

Fig. 9. Representation of the Rossby number (R_o) for the gradient flow versus the Burger number (B') for the change in interface height across the ring (solid line). (a) Evolution of 2G1, 2G2, and 2G3 (b) Evolution of RE11.

RE11 are initially slightly off balance, but then adjust and closely follow the scaled gradient balance curve (Figures 9a and 9b).

In a two-layer configuration, assuming the lower layer to be at rest, Olson et al. [1985] found that the direct surface velocity measurements of observed rings were consistently higher than those predicted by the gradient balance relation of (4) (Figure 10a). They suggested that the difference is due either to surface effects or to coherent barotropic modes. A potential source of error is the influence of azimuthal averaging of h and v in (4). As mentioned earlier, this effect is small and thus the difference is real [Olson et al., 1985]. A similar result is obtained for RE11, even when the contribution of the second interface displacement to the gradient velocities is taken into account, the bottom layer being at rest. In this latter case, the top layer gradient velocities are derived from

$$\frac{v_1^2}{r} + fv_1 = \frac{\partial}{\partial r}(g_1' h_1 + g_2' h_2) \tag{9}$$

where g_1', h_1, g_2', and h_2 correspond to the reduced gravity and depth at the first and second interface, respectively, and v_1 is the upper layer velocity. The corresponding velocity profile (model, gradient and geostrophic) of the upper layer of RE11 for day 2955 and day 3005 are displayed in Figure 10b. The upper layer geostrophic velocity is computed as follows:

$$fv_{g_1} = \frac{\partial}{\partial r}(g_1' h_1 + g_2' h_2) \tag{10}$$

One can therefore ask to what extent the approximation of a lower layer at rest is valid. Equation (4) can be rewritten as
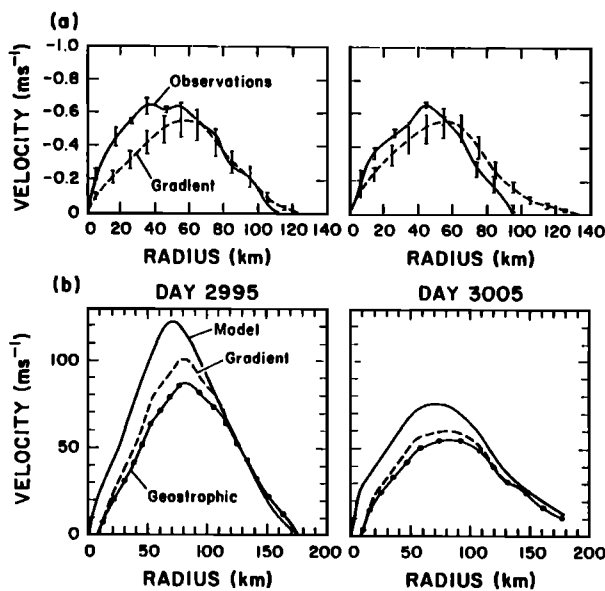
$$\frac{v^2}{r} + fv = fv_g \tag{11}$$

Fig. 10. Velocity profiles (a) for ring 82B in April-May and June (solid line for observations and dashed for gradient) [after Olson et al., 1985] and (b) for RE11 for day 2955 and day 3005 (solid line for model velocities, dashed line for gradient and dotted line for geostrophic).

where v_g is the total geostrophic velocity. For example, at day 2955 (Figure 10b), the observed maximum velocity in the upper layer is $v \sim 1.2\,\mathrm{m\,s}^{-1}$ and from (11), this leads to $v_g \sim 1\,\mathrm{m\,s}^{-1}$. The derived geostrophic velocity from (10) is $\sim 0.85\,\mathrm{m\,s}^{-1}$ (Figure 10b), which implies barotropic velocities of the order of $0.15\,\mathrm{m\,s}^{-1}$ in the lower layer (previously at rest) to maintain the balance. This is effectively the case right underneath the ring. The same reasoning is valid for the other periods. The difference between the gradient velocities calculated assuming the lower layer at rest and the model velocities is the barotropic component of the flow. If the lower layer is considered to be at rest, the upper layer velocities of the ring are underestimated by about 10%. The model rings therefore have a coherent structure to the bottom. This may also be the case for observed rings, since surface velocities are found to be higher than those predicted by the gradient balance assuming the lower layer at rest [Joyce, 1984; Olson et al., 1985; Olson and Evans, 1986]. In fact, recent observations from a 2-year deployment of an array of current meter moorings in the Agulhas retroflection region suggest that both the retroflection and Agulhas rings have very strong (99%) coherence in the vertical from the bottom to the surface (J. R. Luyten, personal communication, 1988).

3.2. Ring Translation Speeds

Gulf Stream rings were found to have translation rates up to 10 times faster [Brown et al., 1986] than those expected for an equivalent upper-layer isolated eddy from either the early theory of Flierl [1977] or the models of Nof [1981, 1983]. Advection by the larger scale mean circulation and interactions with the Gulf Stream were suggested to account for the difference. Furthermore, this behavior is not restricted to Gulf Stream rings. Olson and Evans [1986] compared the translation speed of two Agulhas rings surveyed in November-December 1983 to Flierl and Nof's estimate. They found the observed translation rate to be approximately 2 to 5 times faster. This was also attributed to advection by the larger scale flow.

The model rings (2G1, 2G2, 2G3, and RE11) also exhibit this more rapid motion. Their propagation speeds are of approximately the same magnitude as their observed counterparts: $\sim 9\,\mathrm{cm\,s}^{-1}$ for 2G1, 2G2 and 2G3 versus $6.5\,\mathrm{cm\,s}^{-1}$ for long-lived Gulf Stream anticyclonic rings [Brown et al., 1986] and $5\,\mathrm{cm\,s}^{-1}$ for Gulf Stream cyclonic rings [Richardson, 1980]; in the Agulhas case, $6.2\,\mathrm{cm\,s}^{-1}$ for RE11 versus $4.8\,\mathrm{cm\,s}^{-1}$ and $8.5\,\mathrm{cm\,s}^{-1}$ from two observed Agulhas rings [Olson and Evans, 1986]. Frequent changes in the ring translation speeds were observed in series of observations of warm-core rings [Brown et al., 1983; Cornillon et al., 1989]. In the particular case of 82B, Brown et al. [1983] suggested that it may be related to an adjustment process that the ring undergoes during its interaction with the Gulf Stream. Model ring 2G3 shows a similar behavior as its westward translation speed increases from 6 to 11 cm s^{-1} as it moves away from the mid-latitude jet. Some of the factors affecting the ring propagation are discussed in section 4.

3.3. Ring APE and KE

The depth of the isotherm considered to be the best fit to the main thermocline can also be used within the context of

the two-layer model of the observed ring's structure [*Olson et al.*, 1985] to compute kinetic and available potential energy. The same calculation can be performed with the model rings by using the first interface depth (which corresponds approximately to that of the chosen isotherm, as shown previously). Upper layer kinetic energy (K), available potential energy associated with the first interface (P) and corresponding volume are calculated with a mean radial profile computed over the ring. The ring is assumed to be symmetric. Deviations from this assumption are discussed below. The energy content of several modeled and observed rings at some instant are presented in Table 3. In this particular case, 2G1, 2G2, and 2G3 are more energetic than 82B and CCR76. On the other hand, the model Agulhas rings are smaller and less energetic than the two counterparts observed in November-December 1983.

The time decay of available potential (P) and kinetic (K) energies for the rings 2G1, 2G2, 2G3, and RE11 are presented in Figure 11. The available potential energy P is based on the layered formulation

$$P = \frac{1}{2}\rho g' \int (h - h_\infty)^2 dA \qquad (12)$$

where ρ is the upper layer density, g' is the reduced gravity at the interface, h is the depth of the first interface, and h_∞ is the outside reference. For the estimates of P presented in Table 3, h_∞ is assumed to be the level of the thermocline (or interface) outside of the influence of the ring. In view of the limited size of the domain and of the proximity of the mid-latitude jet, this is not an absolute reference level for the energetics and a small change in h_∞ (defined as a function of time) will have a significant impact on the estimate of P. Rings 2G1, 2G2, and 2G3 do not have a regular decay in P (Figures 11a and 11b) and this can be attributed to the proximity of the mid-latitude jet. In the case of RE11, once it is away from the influence of the African continent, its available potential energy P has an exponential-type decay (Figure 11d). In contrast, the decay in K is fairly regular for all four rings 2G1, 2G2, 2G3, and RE11.

In order to facilitate comparisons among observations and model rings, the top layer decay time scales (τ_P, τ_K) for a certain period can be calculated by dividing the energy content of the ring, as calculated above by the time rate of change of each quantity over the time period. Model ring time decays ($\sim$ 100-200 days for τ_P and τ_K for a 60-day time period when applicable) are found to be much faster than observed ones. In the case of the Gulf Stream ring 82B [*Olson et al.*, 1985], the decays were found to depend strongly on the ring proximity to the Gulf Stream. When the ring is outside the Gulf Stream and topographic influences, the τ_P decay scale is $\sim$ 500 days (compared to 600 and 520 days for cyclonic rings [*Olson*, 1980]). When the rings interact with the stream, large energy losses occur [*Olson et al.*, 1985]. Some of the factors affecting the ring decay are discussed in more detail in section 4.

4. FACTORS AFFECTING RING MOTION AND EVOLUTION

As already stated in section 1, a successful intercomparison between observed and modeled rings provides the opportunity and justification to isolate in the model the possible factors influencing the observed ring motion and

evolution, which is not possible with observations alone. The differences can be rationalized in terms of model initial conditions (domain size, forcing, stratification, etc.) as well as shortcomings of the physics used. In particular, at this stage of the comparison, the model vertical structure is certainly highly simplified in terms of what might be required to realistically simulate oceanic rings. One has also to keep in mind that only a few observed and modeled rings have been compared here. More long time in situ observations are needed. Nevertheless, a good agreement is obtained in terms of thermocline depth, ring size, swirl velocities, and translation speeds.

In this section, some of the issues addressed in the previous section are investigated by running and comparing several subsidiary experiments. The first one considers the importance of the external flows on the ring propagation, while the second discusses the importance of the lateral viscosity used in the model on the rings decay. Because of the more isolated nature of RE11 (less interaction with an external jet and a longer lifetime than 2G1, 2G2, and 2G3), the specific case of this ring is studied in detail.

4.1. Ring R1: Advection by Larger Scale Flows

In order to study the influence of the larger scale flows, the ring RE11 is first extracted from E11 at day 2965. The position of the center was estimated and u, v, and h in each layer were saved within a radius of 150 km (distance from the center to the tip of Africa). The model, configured in the same basin, is then initialized with RE11 only and no wind forcing is applied (Table 4). The initial conditions in the ring, now referred to as R1, are interface displacements and velocities of RE11 in each layer. One of the limitations of such an approach is that the ring, once extracted, will have to readjust initially to its motionless environment and therefore will be somehow different from RE11.

The time evolution of R1 for a period of 200 days is illustrated in Figure 12. The ring is initially in contact with the African continent and generates a Kelvin wave along the eastern coast of Africa, leaving a strip of current behind it. This Kelvin wave propagates cyclonically around the basin (southern hemisphere). The measured wave speed is of the order of $2\,\mathrm{m\,s^{-1}}$, which is between the first and second baroclinic mode Kelvin wave propagation speeds (2.7 and $1.7\,\mathrm{m\,s^{-1}}$, respectively, with $c_{Kelvin} = fR_d$). The internal Rossby radii of deformation (R_d) are computed following *Lighthill* [1969] and assuming the at-rest stratification. Equivalent depth values of 74.2 and 27.4 cm are obtained for the two baroclinic modes, corresponding to radii (R_d) of 27 and 16 km, respectively. As this pressure disturbance reaches the eastern boundary, it excites a wave whose western edge progresses at a speed of approximately $1.5\,\mathrm{cm\,s^{-1}}$, which is of the order of the long Rossby wave speed βR_d^2, as expected (1.5 and $0.5\,\mathrm{cm\,s^{-1}}$ for the first and second baroclinic modes, respectively). Because of the small basin size, the Kelvin wave can propagate around the entire basin and form a closed circulation (Figure 12c).

The ring R1 initially moves westward until day 40 and northwestward thereafter, leaving a trail of Rossby waves in its wake [*Flierl*, 1977, 1984]. It is only after day 150 (Figure 12f) that the ring detaches from the African continent. The direct westward propagation of R1 during the first 40 days (Figure 12h) is at a speed of $\sim 3.6\,\mathrm{cm\,s^{-1}}$ (Table 5).
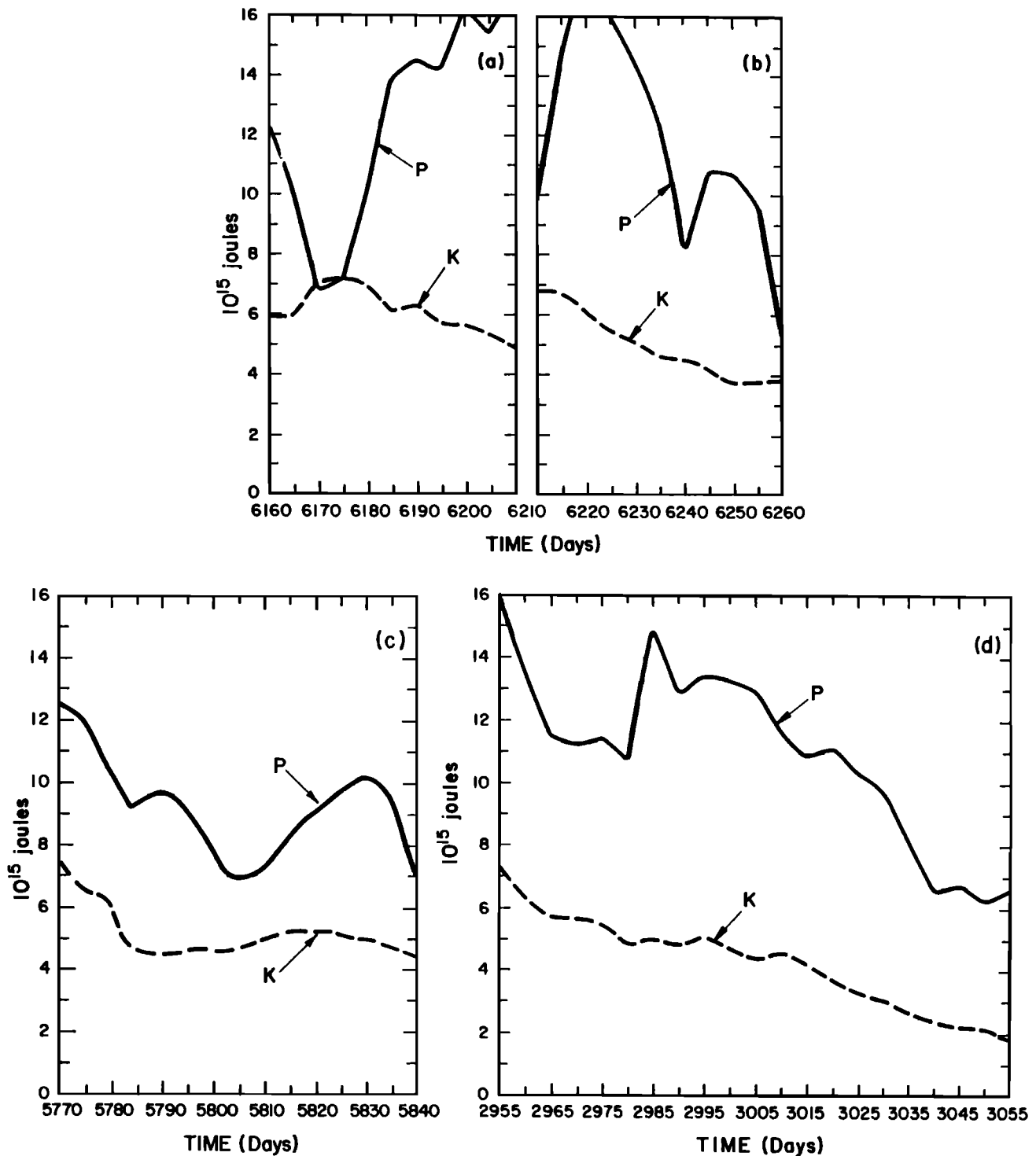
Fig. 11. Time decay of available potential energy P and kinetic energy K for (a) 2G1, (b) 2G2, (c) 2G3, and (d) RE11.

This is close to the initial $4.3 \, \mathrm{cm \, s^{-1}}$ of RE11, suggesting that external flows exert only a small influence on the propagation of RE11 during its passage from the Indian to the Atlantic basin. This is not surprising since there is almost no mean flow connecting the two basin circulations. After 40 days, R1 decelerates and moves northwestward at a speed $\sim 2.2 \, \mathrm{cm \, s^{-1}}$ (Table 5). This propagation speed is much slower than that of RE11 $(6.2 \, \mathrm{cm \, s^{-1}})$, suggesting a

strong influence of the South Atlantic subtropical gyre on the movement of the latter.

In order to further investigate the latter point, one needs estimates of the velocities of the surrounding water. *Cornillon et al.* [1989] determined the mean velocity of the slope water surrounding Gulf Stream warm-core rings using a combination of in situ observations with a depth weighting based on theoretical arguments. They found

TABLE 4. Parameters of the Experiments.

Ring	Number of Layers	Thickness of Layers, m	g', ms^{-2}	Bottom Drag, s^{-1}	African Continent (Yes or No)	Basin Size, km × km	Initial Conditions
R1	3	300 900 3800	0.02 0.005	10^{-7}	Yes	2520 × 1280	ring extracted from E11, no wind forcing.
R2					No		as R1, but no Africa
R3							as R2, but $A_M = 100\,m^2s^{-1}$
R4							as R2, but $A_M = 50\,m^2s^{-1}$
R5							as R2, but $A_M = 25\,m^2s^{-1}$

For all experiments, $\Delta x = 20$ km. Blanks indicate no change from the previous experiment.

that the ring propagation relative to the slope water was $4.6 \pm 3.0\,cm s^{-1}$ for a mean translational velocity of the rings of $8.5 \pm 3.1\,cm s^{-1}$. In the numerical model, the mean velocity associated with the South Atlantic subtropical gyre is $\sim 4\,cm s^{-1}$ therefore implying that RE11 propagates at $\sim 2\,cm s^{-1}$ relative to its environment in agreement with Flierl and Nof's estimate.

4.2. Ring R2: Influence of African Continent

In order to investigate the influence of the African continent on the ring propagation, an experiment without Africa, R2, otherwise similar to R1, was run (Table 4). Its time evolution is presented in Figure 13. The ring propagates in a northwestward direction, as expected from previous numerical studies [McWilliams and Flierl, 1979; Mied and Lindemann, 1979; Flierl, 1984] and also leaves a trail of Rossby waves in its wake. This wake is of the same order of magnitude in size and intensity as for R1.

During the first 40 days, R2 propagates toward the west at a speed of the order of $2.7\,cm s^{-1}$ (Table 5), suggesting an influence from the African continent on the westward propagation speed of R1 of the order of $1\,cm s^{-1}$. The total speed of R2 for this period is $\sim 3.4\,cm s^{-1}$ (which is approximately equal to that of R1), with a northward component of $2.1\,cm s^{-1}$. This direction of motion (north) was not allowed in R1, due to the African continent.

It is apparent that the presence of Africa in R1 influences the ring propagation and enhances the westward movement over that due to β. Sommerfeld [1950] showed that the interaction of a point vortex with a lateral boundary is analogous to the interaction of neighboring vortices of opposite sign. The analytical solutions which describe the resulting motion of two-point vortices are well known and are a function of the circulation and the separation distance [Sommerfeld, 1950]. The problem becomes considerably more complex if the point sources are replaced by finite area vortices, so that the vortices may exchange mass [Hooker, 1987].

As described by Sommerfeld, the vortex is pushed forward by its virtual image obtained by reflection in the wall. This theory implies maximum velocities at the boundary and therefore might be applicable in numerical models only when a free-slip boundary condition is used. When a no-slip condition is prescribed, this mirror image

theory breaks down, since the velocities are identically zero at the boundary. However, propagation along the wall in the same direction as for the effect of a virtual image has been observed in numerical experiments using no-slip boundary conditions [Cox, 1979; Smith, 1986]. Cox suggested that, by virtue of the no-slip condition, a narrow but intense band of vorticity of sign opposite to that of the eddy is present between the wall and the eddy and, considering the interactive effects of neighboring vortices [Sommerfeld, 1950; Hooker, 1987], this results in an alongshore movement of the eddy. It is surmised here that such an interaction may account for the differences between the propagation speeds of R1 and R2. This topic is under further investigation in a separate study focused on eddy-wall interaction.

The westward propagation speed of R2 remains the same after the first 40 days, but the northward component decreases sharply, as if the initial period was one of adjustment to the environment (Table 5). The meridional drift is caused both by a form drag exerted by the lower layer and by interactions with the Rossby wave wake of the upper layer [Flierl, 1984]. Since the Rossby-wave radiation in the upper and lower layers and associated form drag cause the eddy to loose energy, the eddy tend to approach its so-called "latitude of rest" [Larichev, 1983] where, owing to changes in the planetary vorticity, their relative vorticity and hence kinetic energy vanish. The propagation speed of R2 is of the same magnitude as of R1 and much slower than of RE11, confirming the strong influence of the South Atlantic subtropical gyre on the movement of the latter.

4.3. Influence of Lateral Eddy Viscosity A_M on Ring Decay

One of the major differences between observed and modeled rings is in their decay rates. The decay rates of the model rings were found in section 3 to be 4-6 times faster than in observed rings. In their study of quasigeostrophic isolated vortices, McWilliams and Flierl [1979] found that the vortex amplitude decay rate, in the limit of strong nonlinearity, is governed by the frictional coefficient rather than dispersion. An important question to consider here, then, is how much of the model ring decay is due to Rossby wave radiation (horizontal and vertical) as compared to viscous dissipation. In the case of an inviscid upper layer lens in the same parameter range as one of those studied here (RE11), Flierl [1984] found a
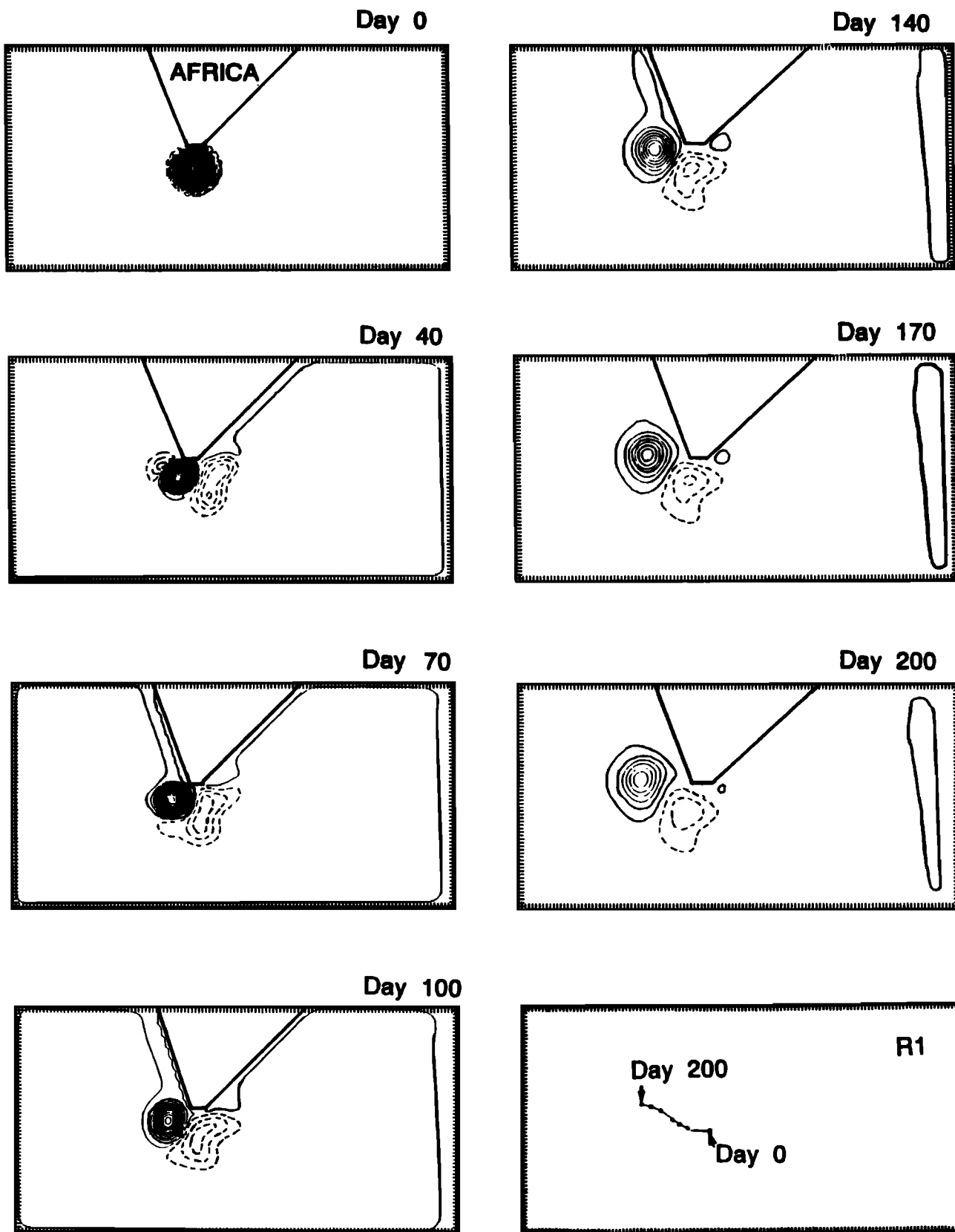
Fig. 12. Upper layer interface displacement anomaly of R1 for a period of 200 days. The contour interval is 10 m and the contour values straddle zero symmetrically. The distance between each tick mark is 20 km.
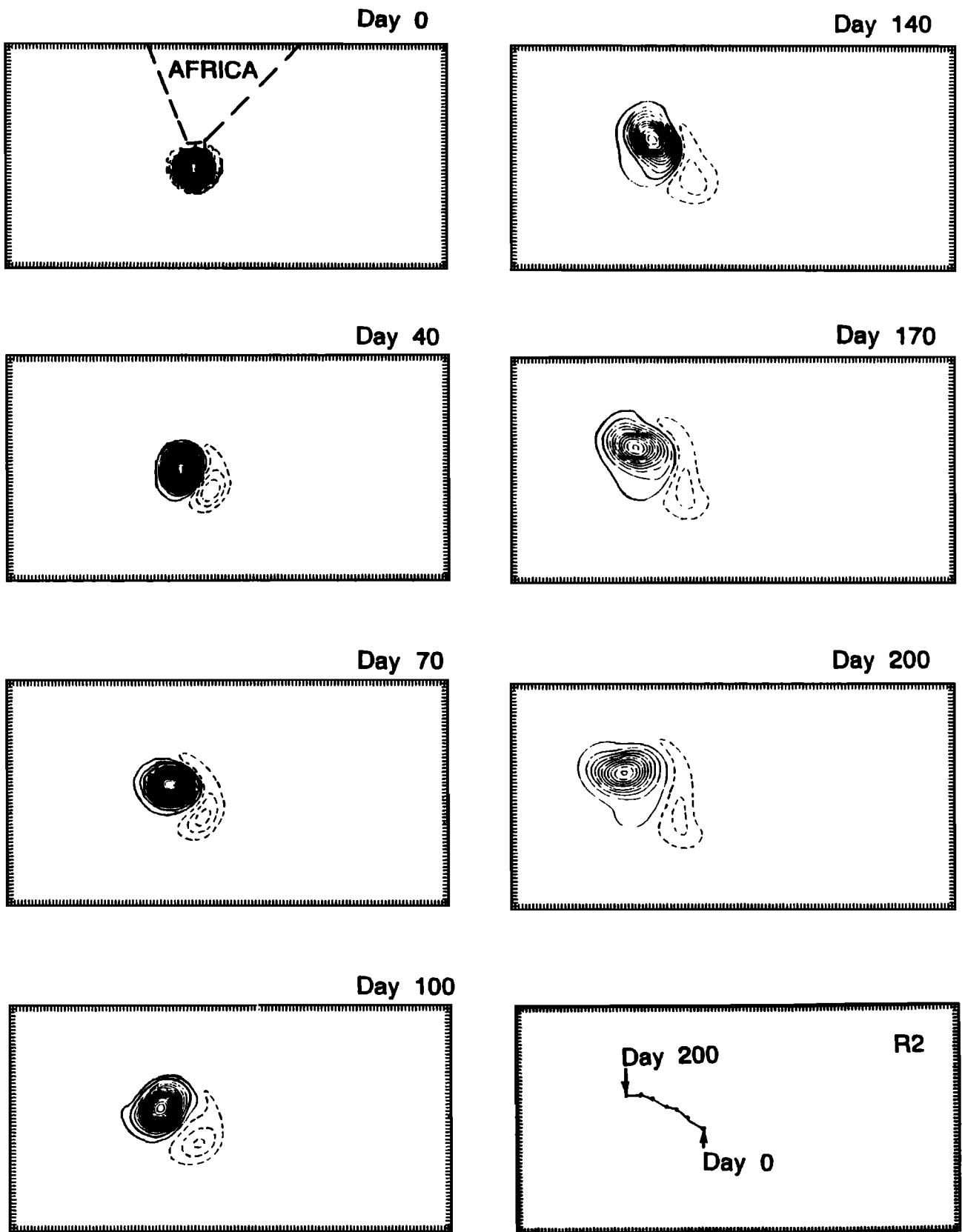
Day 0

Day 140

Day 40

Day 170

Day 70

Day 200

Day 100

Fig. 13. Same as in Figure 12 for R2.

TABLE 5. Ring Propagation Speeds.

Ring	c_{West}, cm s^{-1}		c'_{North}, cm s^{-1}		c_{Total}, cm s^{-1}	
RE11	4.3	5.5	0	2.8	4.3	6.2
R1	3.6	1.9	0.4	1.1	3.8	2.2
R2	2.7	2.6	2.1	1.0	3.4	2.7

The first number in each column corresponds to the propagation speed averaged over the first 40 days; the second number corresponds to the propagation speed after the first 40 days.

decay of the order of 7 years ($\sim$ 2500 days) due to Rossby wave radiation in the lower layer. This is at least one order of magnitude slower than the decay rates obtained in the model. Thus it seems most likely that, as shown by McWilliams and Flierl [1979], viscous effects are the predominant energy sink.

In order to investigate the latter point, three experiments (R3, R4, and R5) identical to R2, except for the value of A_M, were performed (Table 4). The time evolution of the first interface available potential energy (P) and of the upper layer kinetic energy (K) are presented in Figure 14 for R2, R3, R4, and R5. The small differences in P and K at day 2965 for RE11 in Figure 11c and at day 0 for R2 in Figure 14 are due to the differences in the way the computation was performed in each case (the first one assumed the ring to be symmetric, while the second took all the available data into account), and also, in the case of K, due to the presence of the barotropic mode in the velocity field in Figure 14 (see section 3.1 for more detail). The corresponding decay time scales τ_P and τ_K of R2, R3, R4, and R5 as a function of the lateral eddy viscosity A_M over a period of 60 and 100 days are presented in Table 6. The 60-day time period was chosen to be comparable with the values computed for Gulf Stream ring 82B by Olson et al. [1985]. A reduction in the magnitude of A_M by a factor of 6 yields to a doubling of the ring decay time scale, thus illustrating the importance of the viscous effects.

The decay of the above numerical rings can be discussed with the help of a fairly simple energy balance model. In the absence of any diffusion of thermodynamic properties; i.e. thickness in the context of the current simulations, the energy equations can be written as

$$\frac{dK}{dt} = -\mathbf{V}\cdot\nabla_s p - \mathbf{V}\cdot\mathbf{k}\rho g + \mathbf{V}\cdot A_M\nabla_s^2\mathbf{V} \qquad (13)$$

$$\frac{dP}{dt} = \mathbf{V}\cdot\nabla_s p + \mathbf{V}\cdot\mathbf{k}\rho g \qquad (14)$$

The kinetic energy balance can then be expressed as

$$\frac{dK}{dt} = -\frac{dP}{dt} + \mathbf{V}\cdot A_M\nabla_s^2\mathbf{V} \qquad (15)$$

There are two basic scenarios which act as limiting cases for an analysis of the numerical results. The first one is when the change in available potential energy matches the dissipation; i.e.

$$\frac{dP}{dt} = \mathbf{V}\cdot A_M\nabla_s^2\mathbf{V} \quad \Rightarrow \quad \frac{dK}{dt} = 0 \qquad (16)$$

This balance has been suggested for some periods in ring decay based on observations [Olson, 1980; Olson et al., 1985]. These periods coincide with time when the rings are evolving without any major interactions with other current regimes. However, it should be kept in mind that the measures of kinetic energy in the observed rings are poor. This type of evolution is consistent with quasi-geostrophic scaling, which suggests that the ring horizontal length scale L (defined as $R_d(P/K)^{\frac{1}{2}}$ [Pedlosky, 1979]) approaches the internal Rossby radius of deformation R_d as the ring decays [Olson et al., 1985]. The other limit consists of a diffusion dominated state where the rate of avalaible potential energy decay is smaller than that of kinetic energy. The ring then spreads out through momentum diffusion, and the scale of the ring as compared to R_d as well as the ratio P/K increase.

In the above experiments, the simulations clearly tend toward the second limit; i.e. the ratio P/K increases in all experiments (Figure 15a). The length scale associated with the quasi-geostrophic scaling L is also represented and the accompanying increase in ring scale is consistent with the increase in P/K.

If the time rate of change of P and K are assumed to be proportional to the available potential energy P and kinetic energy K themselves, then the governing solution is

$$P = A_o \exp^{-\alpha t}, \quad K = K_o \exp^{-\gamma t} \qquad (17)$$

This is clearly an ad hoc assumption based on the exponential nature of the curves of Figure 14, whose validity will rest in its application. The P and K decay for rings R2, R3, R4, and R5 are again displayed in Figure 15b, but in natural log coordinates. The fits of (17) to the numerical results are extremely significant and improve for lower viscosities. The coefficients α and γ are displayed in Figure 15b.

RE11 and R2 have comparable decay time scales on the 100-day time period (Table 6). However, the decay is faster in R2 over the 60-day time period. This is interpreted as the effect of an initial adjustment of R2 to the motionless environment at day 0. It is only when A_M is less than or equal to 50 m^{2}s^{-1} that the ring decay time scale is of comparable magnitude to the observations. One can therefore ask the question to what extent is this result applicable in the context of the full model (wind stress and African continent). A lateral eddy viscosity of 25 – 50 m^{2}s^{-1} (instead of the current 330 m^{2}s^{-1}) might bring comparable decay times between the modeled and observed rings.

In order to explore this point, two experiments E12 and E13 ($A_M = 100$ and 50 m^{2}s^{-1}, respectively, otherwise similar to E11), were run. With the current grid resolution of 20 km, E13 became numerically unstable after half a year of integration, while E12 remained stable. In the framework of this numerical model, smaller viscosities than 100 m^{2}s^{-1} can be employed only with a reduction in grid spacing to perhaps one-half. A typical ring of E12, named RE12, is analyzed just after its separation from the Agulhas proper and compared to its analog from E11, RE11. The mean vertical profiles of both rings averaged over 100 days are presented in Figure 16. The most striking difference between the two is their size. RE11 was already found to be small in diameter and volume compared to observations,
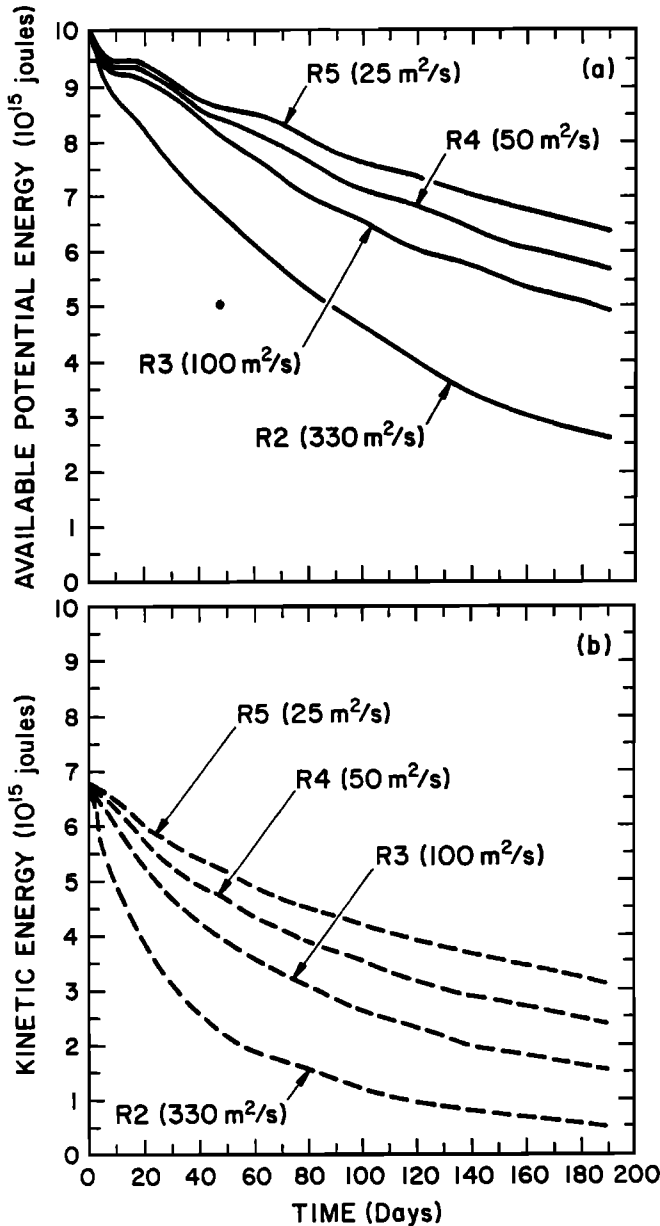
Fig. 14. Time decay of available potential energy P and kinetic energy K for R2, R3, R4, and R5.

TABLE 6. Decay Time Scales τ_P and τ_K for RE11, R2, R3, R4, R5, and 82B When Available.

Ring	A_M, m^2 s^{-1}	τ_P, days		τ_K, days	
RE11	330	190	190	140	135
R2	330	150	190	80	130
R3	100	290	300	125	160
R4	50	400	390	160	210
R5	25	520	500	220	260
82B		500			

The decay time scales weree computed for 60-day and 100-day periods (first and second column, respectively). When applicable, the value of the lateral eddy viscosity A_M is given.

but RE12 is even smaller (diameter $\sim$ 200 km compared to 300 km for RE11). The other major difference is the velocities. The maximum velocities within RE12 are of the order of 250 cm s^{-1} just after separation as compared to 120 cm s^{-1} for RE11. After 50 days, when the ring is away from the African continent, the magnitude of the velocities in RE12 dropped to 200 cm s^{-1} as compared to 75 cm s^{-1} for RE11 and 60 $-$ 90 cm s^{-1} for the observations. The radius of maximum velocities is 55 km in RE12 compared to 80 km in RE11 and $\sim$ 120 km in observations.

The purpose of this exercise was to look at the impact of a smaller lateral eddy viscosity on the ring formation and its decay. Overall, the ring RE12 is smaller and much more intense than RE11 and compares poorly with the observed rings. The corresponding time decay in P and K are presented in Table 7 for both rings RE11 and RE12 once they are away from the influence of the African continent. The decay time scales of RE11 and RE12 are observed to be of the same magnitude (Table 7). In the context of the full model, a change in A_M does not have the impact expected from the isolated rings experiments. The eddy lateral viscosity A_M is therefore not the only factor controlling the ring decay. An additional mechanism to take into account is the interaction of the ring with its environment, which is also affected by the change in A_M.

5. SUMMARY AND DISCUSSION

Rings produced in a two-gyre wind driven circulation model (experiment 2G) and in a model of the South Atlantic/Indian Ocean (experiment E11) have been compared to observed Gulf Stream and Agulhas rings in a consistent fashion through the use of a diagnostic two-layer model. At this stage, the model vertical structure is certainly highly simplified with respect to reality, as might be required to realistically simulate world ocean rings. One also has to keep in mind that these comparisons have been carried out with only a limited number of rings, both observed and modeled. However, a good agreement is obtained between the observed rings main thermocline surface and the first interface depths of the modeled rings when the model mean upper layer thickness (approximation of the mean thermocline depth in the domain) is chosen to be 400 m. Therefore some qualitative comparisons with reality can be made. The model and observed rings exhibit substantial similarity in terms of thermocline depth, ring size, swirl velocities, and translation speeds, in addition to parameters such as the Rossby and Burger numbers. Direct surface velocity measurements in observed rings were found to be consistently higher than those predicted by the gradient balance assuming the lower layer to be at rest, and the same result was obtained for the model rings. In the model, it was demonstrated that this difference is due to the barotropic component of the flow, suggesting that the model rings have a coherent structure to the bottom. There is strong evidence that this is also the case for real oceanic rings.

A successful intercomparison between observed and modeled rings provides the opportunity and justification to isolate in the model the possible factors influencing the observed ring motion and evolution, which is not possible with observations alone. This has been carried out by examining in some detail the motion and evolution of one
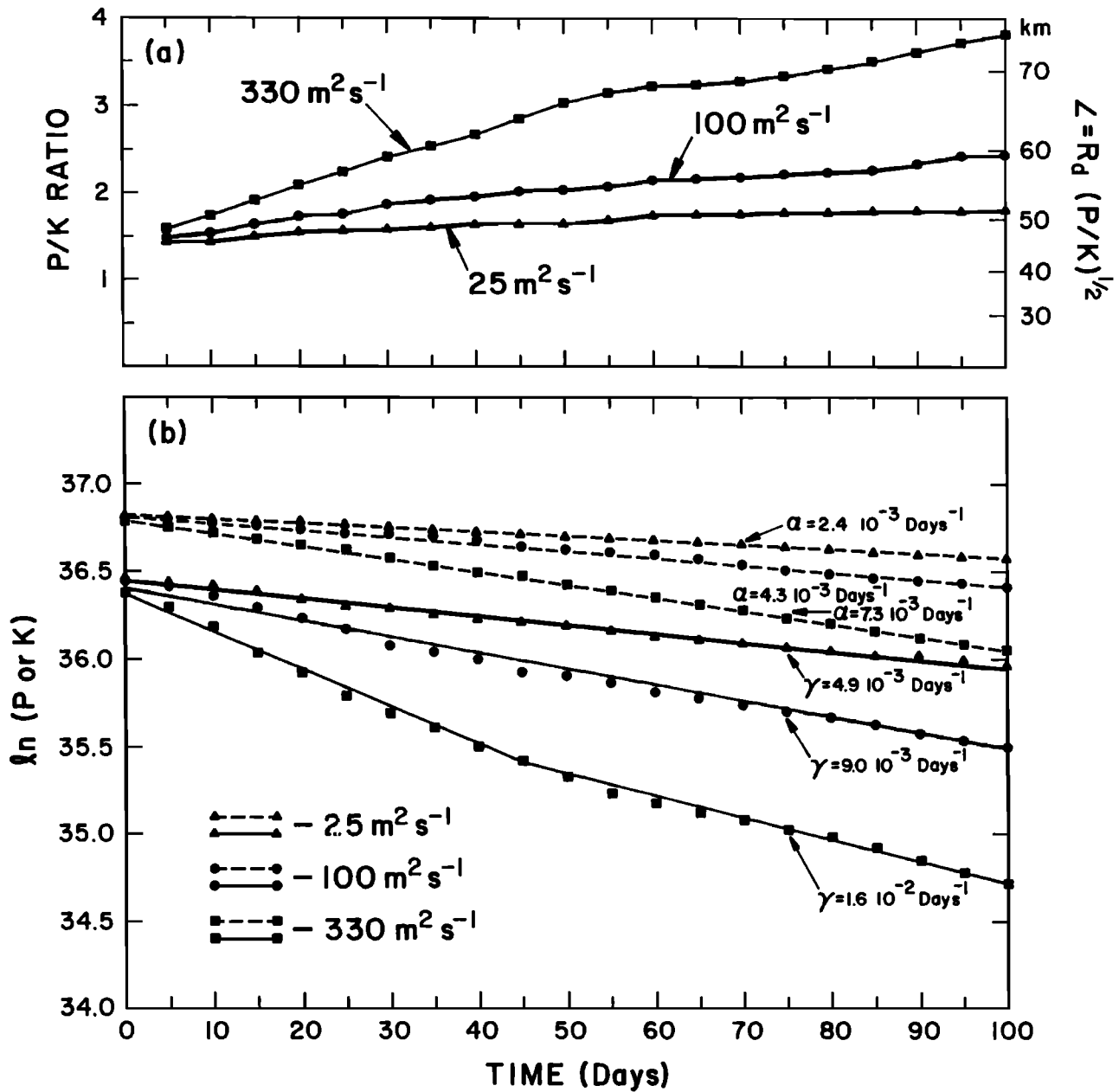
Fig. 15. For R2, R3, and R5: (a) Ratio P/K versus time, $L = R_d(P/K)^{\frac{1}{2}}$, and A_M and (b) $\ln(P)$ (dashed line) or $\ln(K)$ (solid line) versus time and A_M.

ring from the South Atlantic/Indian Ocean model and comparing them with the behavior of a similar ring in each of several subsidiary experiments. It is found that the presence of the African coast provides a westward motion in addition to that due to β, and it seems that this is owing to interaction between the ring and a high vorticity band along the no-slip boundary. There is apparently only a small influence from the external flows on the propagation of the ring during its passage from the Indian to the Atlantic basin due to the absence of continual flow between the two basins. However, the advection by the large-scale flows is found to dominate the motion once the ring drifts into the South Atlantic subtropical gyre.

One of the major differences between observed and modeled rings is in their decay rates. The decay rates of

the model rings were found to be 4 to 6 times faster than in observed rings, and were thought to be strongly influenced by the lateral eddy viscosity present in the model. In order to investigate the latter, several experiments were performed with different values of the lateral eddy viscosity coefficient ($A_M = 330 - 25\,\text{m}^2\text{s}^{-1}$). When isolated, the modeled ring is observed to have an exponential decay in available potential and kinetic energies, as shown by a simple model based on energy balances. It is only when A_M is less or equal to $50\,\text{m}^2\text{s}^{-1}$ that the ring decay scale is of comparable magnitude to the observations. Therefore it seemed likely that the use of a smaller lateral eddy viscosity in the full model (instead of the initial $330\,\text{m}^2\text{s}^{-1}$) will bring a comparable decay time between modeled and observed rings. A reduction of the lateral eddy viscosity
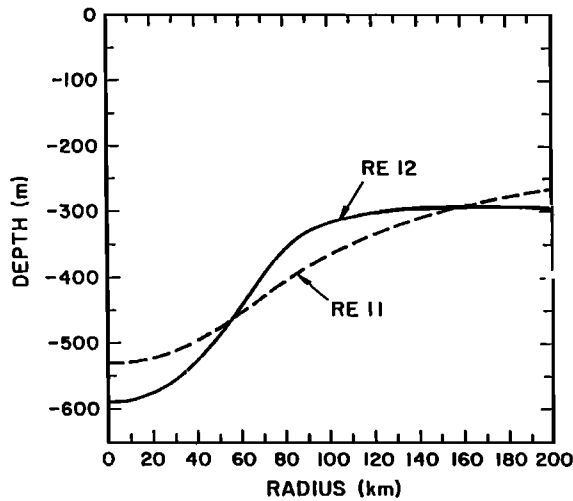
Fig. 16. Vertical profiles averaged over 100 days for RE11 and RE12.

TABLE 7. Decay Time Scales τ_P and τ_K of RE11 and RE12 for a 60-day Period When Away From Influence of African Continent.

Ring	τ_P (days)	τ_K (days)
RE11	120	110
RE12	160	100

coefficient in the full model by a factor of 3 modifies several factors, such as the ring formation process and interaction with the African coast. This induces smaller and more intense rings, but their decay was not affected. Therefore no definite determination can be made as to whether a reduction in the magnitude of the lateral eddy coefficient will, in general, yield better comparison between observed and modeled ring decay rates.

On the one hand, the relative simplicity of the model allowed us to analyze some of the physical mechanisms behind ring propagation, such as advection by the mean flow or boundary influence. On the other hand, the effects of other factors such as basin size, grid spacing and bottom topography/realistic coastline are also felt to be of importance, and the model's simplicity has, thus far, inhibited their determination. It is therefore expected that more insight into ring propagation and evolution can continue to be gained as the realism/complexity of the models is further increased.

REFERENCES

Bleck, R., Finite-difference equations in generalized vertical coordinates, II, Potential vorticity conservation, *Contrib. Atmos. Phys.*, *51*, 360-372, 1979.

Bleck, R., and D. B. Boudra, Initial testing of a numerical model ocean circulation model using a Hybrid (quasi-Isopycnic) vertical coordinate, *J. Phys. Oceanogr.*, *11*, 755-770, 1981.

Boudra, D. B., and E. P. Chassignet, Dynamics of Agulhas retroflection and ring formation in a numerical model, I, The vorticity balance, *J. Phys. Oceanogr.*, *18*, 280-303, 1988.

Brown, O. B., D. B. Olson, J. W. Brown and R. H. Evans, Satellite infrared observation of the kinematics of a warm-core ring, *Aust. J. Mar. Freshwater Res.*, *34*, 535-545, 1983.

Brown, O. B., P. C. Cornillon, S. R. Emmerson and H. M. Carle, Gulf Stream warm rings: A statistical study of their behavior, *Deep Sea Res.*, *33*, 1459-1473, 1986.

Chassignet, E. P., and D. B. Boudra, Dynamics of Agulhas retroflection and ring formation in a numerical model, II, Energetics and ring formation, *J. Phys. Oceanogr.*, *18*, 304-319, 1988.

Cheney, R. E., and P. L. Richardson, Observed decay of a cyclonic Gulf Stream ring, *Deep Sea Res.*, *23*, 143-155, 1976.

Cornillon, P., R. Weyer, and G. Flierl, Translational velocity of warm core rings relative to the Slope Water, *J. Phys. Oceanogr.*, *19*, 1317-1332, 1989.

Cox, M. D., A numerical study of Somali Current eddies, *J. Phys. Oceanogr.*, *9*, 312-326, 1979.

Elliot, B. A., Anticyclonic rings in the Gulf of Mexico, *J. Phys. Oceanogr.*, *12*, 1292-1309, 1982.

Flierl, G. R., The application of linear quasigeostrophic dynamics to Gulf Stream rings, *J. Phys. Oceanogr.*, *7*, 365-379, 1977.

Flierl, G. R., Rossby wave radiation from a strongly nonlinear warm eddy, *J. Phys. Oceanogr.*, *14*, 47-58, 1984.

Gent, P. R., and J. C. McWilliams, Isopycnal mixing in ocean circulation models, *J. Phys. Oceanogr.*, *20*, 150-155, 1990.

Gordon, A. L., and W. F. Haxby, Agulhas eddies invade the South Atlantic - Evidence from Geosat altimeter and shipboard CTD, *J. Geophys. Res.*, *95*, 3117-3125, 1990.

Holland, W. R., The role of mesoscale eddies in the general circulation of the ocean - Numerical experiments using a wind-driven quasi-geostrophic model, *J. Phys. Oceanogr.*, *8*, 363-392, 1978.

Hooker, S. B., Mesoscale eddy dynamics by the method of point vortices, Ph.D. thesis, 158 pp., Univ. of Miami, Miami, Fla., 1987.

Iselin, C. O., The influence of vertical and lateral turbulence on the characteristics of the waters at mid-depth, *Eos Trans. AGU*, *20*, 414-417, 1939.

Joyce, T. M., Velocity and hydrographic structure of a Gulf Stream warm-core ring, *J. Phys. Oceanogr.*, *14*, 936-947, 1984.

Joyce, T. M., S. L. Patterson, and R. C. Millard, Anatomy of a cyclonic ring in the Drake passage, *Deep Sea Res.*, *18*, 1265-1287, 1981.

Joyce, T.M., et al., Rapid evolution of a Gulf Stream warm-core ring, *Nature*, *308*, 837-840, 1984.

Larichev, V. D., General properties of nonlinear synoptic dynamics in the simplest model of barotropic ocean, *Oceanologiya*, *23*, 551-558, 1983.

Lighthill, M. J., Linear theory of long waves in a horizontally stratified ocean of uniform depth (Appendix), *Philos. Trans. R. Soc. London*, *265*, 85-92, 1969.

Lutjeharms, J. R. E., and R. C. van Ballegooyen, The retroflection of the Agulhas current, *J. Phys. Oceanogr*, *18*, 1570-1583, 1988.

McWilliams, J. C. and G. R. Flierl, On the evolution of isolated non-linear vortices, with application to Gulf Stream rings, *J. Phys. Oceanogr.*, *9*, 1155-1182, 1979.

Mied, R. P. and G. J. Lindemann, The propagation and evolution of cyclonic Gulf Stream rings, *J. Phys. Oceanogr.*, *9*, 1183-1206, 1979.

Montgomery, R. B., The present evidence on the importance of lateral mixing processes in the ocean, *Bull. Am. Meteorol. Soc.*, *21*, 87-94, 1940.

Nilsson, C. S., and G. R. Cresswell, The formation and evolution of East Australian current warm-core eddies, *Prog. Oceanogr.*, *9*, 133-183, 1980.

Nof, D., On the β-induced movement of isolated baroclinic eddies, *J. Phys. Oceanogr.*, *11*, 1662-1672, 1981.

Nof, D., On the migration of isolated eddies with application to Gulf Stream rings, *J. Mar. Res.*, *41*, 399-425, 1983.

Olson, D. B., The physical oceanography of two rings observed by

the cyclonic ring experiment, II, Dynamics, *J. Phys. Oceanogr.*, *10*, 514-528, 1980.

Olson, D. B. and R. H. Evans, Rings of the Agulhas, *Deep Sea Res.*, *33*, 27-42, 1986.

Olson, D. B., R. W. Schmitt, M. Kennelly and T. M. Joyce, A two-layer diagnostic model of the long-term physical evolution of warm-core ring 82B, *J. Geophys. Res.*, *90*, 8813-8822, 1985.

Pedlosky, J., *Geophysical Fluid Dynamics*, 624 pp., Springer-Verlag, New York, 1979.

Richardson, P., Gulf Stream ring trajectories, *J. Phys. Oceanogr.*, *10*, 90-104, 1980.

Sommerfeld, A., *Mechanics of deformable bodies*, 396 pp., Academic, San Diego, Calif., 1950.

Smith, D.C, IV, A numerical study of Loop Current eddy interaction with topography in the western Gulf of Mexico, *J. Phys. Oceanogr.*, *16*, 1260-1272, 1986.

Vastano, A.C., J.E. Schmitz, and D.E. Hagan, The physical oceanography of two rings observed by the cyclonic ring experiment. Part I: Physical structure, *J. Phys. Oceanogr.*, *10*, 493-513, 1980.

E. Chassignet and D. B. Olson, Rosenstiel School of Marine and Atmospheric Science, University of Miami, 4600 Rickenbacker Causeway, Miami, FL 33149.